ACS APPLIED MATERIALS & INTERFACES

www.acsami.org

Research Article

Reconfigurable Integrated Optofluidic Droplet Laser Arrays

Han Zhang, Prithviraj Palit, Yonghao Liu, Seyedmohsen Vaziri, and Yuze Sun*

Cite This: *ACS Appl. Mater. Interfaces* 2020, 12, 26936–26942

Read Online

ACCESS | Metrics & More | Article Recommendations | Supporting Information

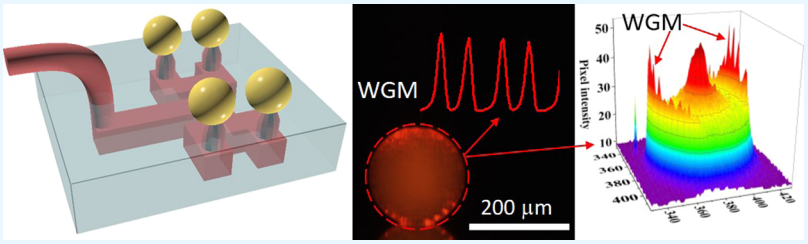

ABSTRACT: Optofluidic lasers are an emerging technology for the development of miniaturized light sources and biological and chemical sensors. However, most optofluidic lasers demonstrated to date are operated at the single optical cavity level, which limits their applications in high-throughput biochemical sensing, high-speed wavelength switching, and on-chip spectroscopic analysis. Here, we demonstrated an optofluidic droplet laser array on a silicon chip with integrated microfluidics, in which four individual droplet optical cavities are generated and controlled by a 2 × 2 nozzle array. Arrays of droplets with a diameter ranging from 115 to 475 μm can be generated, removed, and regenerated on demand. The lasing threshold of the droplet laser array is in the range of 0.63−2.02 $\mu J/mm^2$. An image-based lasing threshold analysis method is developed, which enables simultaneous lasing threshold measurement for all laser units within the laser array using a low-cost camera. Compared to the conventional spectrum-based threshold analysis method, the lasing threshold obtained from the image-based method showed consistent results. Our droplet laser array is a promising technology in the development of cost-effective and integrated coherent light source on a chip for point-of-care applications.

KEYWORDS: *optofluidics, droplet lasers, dye lasers, laser array, whispering gallery mode*

INTRODUCTION

Optofluidic lasers, which utilize different types of optical cavities and have easy access to the gain medium, have been an emerging technology in recent years. Advances in optofluidic lasers have been achieved in the development of miniaturized coherent light resources,[1−4] biological and chemical sensing,[5−7] and bioimaging.[8] To date, optofluidic lasers have been achieved in optical ring resonators,[2,3] distributed feedback gratings (DFB),[4] Fabry−Perot (F−P) cavities,[9] photonic crystals,[10] and random laser systems.[11] However, most of these optofluidic lasers are demonstrated at the single optical cavity level. The development of optofluidic laser arrays on a chip has been largely unexplored. Because of the adaptive nature of the liquids, optofluidic laser arrays possess unique advantages for application in high-speed wavelength switching light sources,[2,12−14] on-chip spectroscopic analysis,[15−17] and high-throughput biochemical sensing systems.[18−20] In the last 2 decades, Oki et al. first demonstrated a DFB grating-based dye laser array and performed digital spectroscopy without wavelength scanning.[21] Maeda et al. improved the DFB dye laser array and achieved high-speed wavelength switching through acousto-optic and thermo-optic effects.[12] Oki et al. demonstrated a flow cytometry chip combined with multiple DFB dye lasers, potentially for biological analysis and medical diagnosis.[17] Meanwhile, laser arrays made of traditional solid-phase materials with various types of optical cavities, such as photonic crystals,[14] F−P cavities,[9] and microdisks,[20] have been developed for high-throughput biological and chemical sensing.

Solid-phase laser arrays are robust, easy to fabricate, cost-competitive, and highly integrable. However, because of the nature of the material, the structure and dimension of these optical cavities are fixed once the device is fabricated. Without introducing external effects, the laser arrays have a rather limited tuning capability. In contrast, a liquid optical cavity, that is, a droplet, can be reconfigurable and dynamically tuned and controlled by novel microfluidic designs,[22,23] evaporation/condensation kinetics,[24] interfacial tension,[25] ultrasonic waves,[26] heating,[27] and pressure.[28] A microdroplet has a nearly perfect spherical geometry and a smooth surface as a result of minimization of interfacial energy, which facilitates to

Received: March 31, 2020
Accepted: May 21, 2020
Published: May 21, 2020

https://dx.doi.org/10.1021/acsami.0c05967
ACS Appl. Mater. Interfaces 2020, 12, 26936−26942

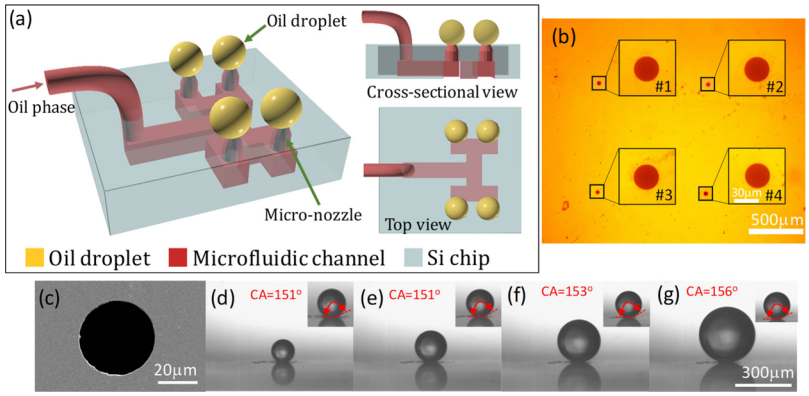

Figure 1. (a) Schematic of droplet laser arrays on a silicon chip. The main channel splits into four equal branches to guide the fluid into the 2 × 2 micronozzle. (b) Optical microscopy image of the nozzle array with a zoom-in view of each nozzle. (c) SEM image showing the size of a nozzle as 30 μm in diameter. (d–g) Droplets of different sizes generated on a nozzle. The droplet diameters are 126, 175, 233, and 303 μm, respectively. The CA of all droplets is larger than 150°, which indicates that the droplets have a minimal contact with the substrate surface.

achieve a low lasing threshold. Additionally, with a proper cavity design, a microdroplet inherently provides a liquid environment, which is compatible with biological materials, such as cells, DNAs, and proteins, and thus presents potential for biosensing applications. Currently, microdroplet lasers have been demonstrated either in microfluidic channels[2,22,29,30] or in a static system.[31−36] Microdroplet lasers in a static system that are supported on superhydrophobic or superhydrophilic surfaces have been demonstrated by spraying[36] or two-phase solution mixing.[33] This type of microdroplet laser is randomly distributed on a substrate surface, presenting a large size distribution, and is not easy to be further manipulated after generation. Additionally, it is challenging to develop controlled droplet laser arrays out of this platform. Microdroplet lasers in microfluidic channels, on the other hand, have a highly monodispersed size distribution of the droplet cavity.[2,22,29,30] However, each droplet is generated and flows sequentially in the microfluidic channel; thus, the multidimensional spatial arrangement of multiple droplets is challenging and limited by the fluidic channel geometry.

Considering the unique advantages of microdroplet lasers, here we demonstrate for the first time, to the best of our knowledge, an optofluidic droplet laser array on a chip using a silicon-based micronozzle platform. A 2 × 2 droplet laser array is fabricated and studied in this work as a proof of concept. However, the device can be readily scaled up to a higher density laser array on a silicon chip through standard photolithography and soft lithography. The lasing property of single droplets from the droplet array has been investigated. The lasing threshold for the droplets with their diameter varying from 115 to 475 μm is in the range of 0.63−2.02 μJ/mm^2. Because of the array arrangement of microdroplets, it is challenging to record all the emission spectra for each droplet simultaneously through one spectrometer. Therefore, an image-based analysis method is developed to measure the lasing threshold of all droplets in the array simultaneously. A comparison study shows that the threshold value obtained from the image-based analysis is highly consistent with the one obtained from spectrum-based analysis. The average lasing thresholds achieved by spectrum-based analysis and image-based analysis, respectively, are within 6.68% difference from each other. The accuracy of the image-based lasing threshold analysis method can be further improved by increasing the resolution of the camera. Additionally, the image-based analysis enables a cost-effective way to characterize the laser performance by reducing the use of a high-resolution spectrometer, which is bulky and expensive. The optofluidic droplet laser array and image-based analysis method demonstrated in this work are a promising technology for the development of a cost-effective and integrated coherent light source on a chip for point-of-care applications.

EXPERIMENTAL SECTION

Design. In order to simultaneously generate multiple droplets on a chip, a 2 × 2 micronozzle array and a set of branch-splitting microfluidic channels are designed, as shown in Figure 1a. Each nozzle is connected to its own microfluidic channel located at the backside of the silicon chip. The main channel splits into two equal branches with a symmetric design. Each of these two branches further splits into another two equal branches, at the end of which the micronozzle is located. The size of the nozzle through the hole is 30 μm in diameter. The distance between two adjacent nozzles is 1 mm (center to center). The width of the backside main channel is 500 μm, which tapers down to 200 μm for all subsequent branch channels. The height of the backside channels and the depth of the nozzle holes are 150 μm, respectively. Immersion oil (or a hydrophobic phase material) containing dye molecules is delivered to microfluidic channels through the inlet when the micronozzle array is immersed in water (or a hydrophilic phase material). When a positive pressure is applied to microfluidic channels, the oil phase will emerge from individual nozzles and simultaneously form an array of oil droplets in water. Microdroplets having a refractive index (e.g., immersion oil, n = 1.515) higher than that of the surrounding liquid (water, n = 1.334) and a low absorption coefficient ($\alpha < 10^{-3}$ cm^{-1}) form optical microcavities that support high Q-factor (>10^6)[37,38] whispering gallery modes (WGMs); light emitted from the gain material (i.e., dye) is confined and amplified in the droplets by the total internal reflection at the cavity surface and thus achieve lasing. When oil droplets reach a desired size, water flow is initiated to wash away the droplets, which allows the regeneration of new droplets. The symmetric design of the microfluidic channels helps to maintain the same pressure for every nozzle, so that the droplets generated on each nozzle have the same size. With proper control between the pressurized oil phase and water flow, the generation and regeneration of droplets with different sizes can be easily achieved.

Fabrication of Si Nozzle Devices. Through the standard photolithography technique, the fabrication of a micronozzle array device is outlined in three major steps, as shown in Figure 2a: nozzle through-hole etching from the top side, microfluidic channel etching from the bottom side, and anodic bonding of the Si chip to a glass substrate. Bare Si samples (N/Ph⟨100⟩, 300 ± 25 μm thickness, double-side polished) are immersed in the piranha solution

https://dx.doi.org/10.1021/acsami.0c05967
ACS Appl. Mater. Interfaces 2020, 12, 26936−26942

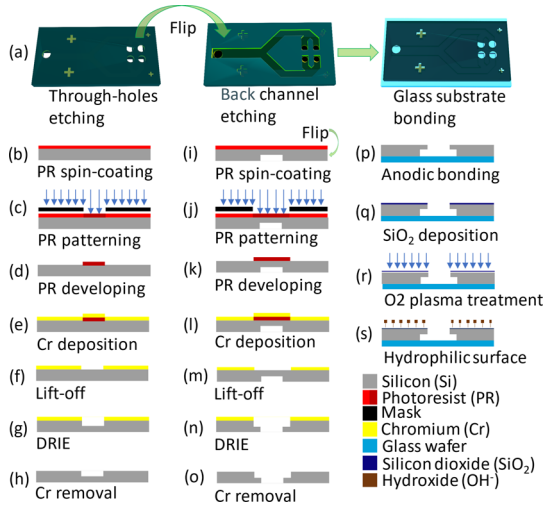

Figure 2. Fabrication process flow for the micronozzle array. (a) Three major steps of fabrication. (b–h) Detailed process for through-holes etching. (i–o) Detailed process for back channel etching. (p–s) Detailed process for glass substrate bonding.

($V_{\text{surfuric acid}}/V_{H_2O_2}$ = 3:1) for 15 min, rinsed with plenty of deionized water, and dried under N_2 flow. The cleaned Si samples are spin-coated with a NR9 negative photoresist (Futurrex) at 500 rpm for 30 s and 4000 rpm for 60 s and then baked at 150 °C for 60 s on a hot plate. The spin-coated Si samples are aligned with a predesigned mask and exposed to UV light at 20 mW/cm^2 power density for 9.5 s under a G-line aligner system (OAI model 800 backside mask aligner). After being baked at 100 °C for 60 s and developed for 65 s with agitation, the patterned Si samples are ready for chromium (Cr) metal mask deposition, which works as a hard mask for nozzle through-hole etching. A 20 nm thick Cr layer is deposited on the patterned Si samples (AJA E-beam evaporator) and the remaining photoresist covered by Cr is lifted off by dipping the Si samples in acetone for 5 min. The final Cr mask-patterned Si samples are etched for 150 μm through deep reactive ion etching (DRIE). After removing the Cr mask, the fabrication of a 2 × 2 micronozzle through holes on the Si samples is finished. The step-by-step process flow is shown in Figure 2b–h. The optical microscopy image of the 2 × 2 nozzle array is shown in Figure 1b, with a diameter of 30 ± 3 μm. The scanning electron microscopy (SEM) image of a fabricated nozzle is shown in Figure 1c. The backside channel etching is performed from the bottom side of Si samples, as shown in Figure 2i–o. After DRIE and Cr mask removal, the final etching depth of the backside channel is 150 μm. Finally, the Si nozzle array samples are bonded to glass wafers using a home-built anodic bonding system, as shown in Figure 2p. To improve the hydrophilicity of the Si nozzle surface, 50 nm thick SiO_2 is deposited on the top surface by plasma enhanced chemical vapor deposition, followed by plasma treatment (100 W, 30 s, and O_2 20 sccm), as shown in Figure 2q–s. The microfluidic channel inlet is created on polydimethylsiloxane that is bonded to the micronozzle device.

Optical Setup. A typical confocal setup is used to excite the droplet array, as shown in Figure 3. The excitation source is an optical parametric oscillator (OPO) pulsed laser at a wavelength of 532 nm (repetition rate: 2 Hz, pulse width: 5–7 ns, pulse energy: 1 mJ per pulse). The pump power is first attenuated by a fixed neutral density filter (OD = 1) and then adjusted by a continuously variable neutral density filter. The power of the OPO laser per pulse is measured with a power meter in real time. The laser excitation beam spot size is around 10 mm^2. The emission light is collected through a 20× objective lens and analyzed by a monochromator (HORIBA iHR320, at a spectral resolution of 0.2 nm). The top-view and side-view images of the droplet are captured by the top-view and side-view cameras (Genie Nano C800, Teledyne DALSA) in real time for droplet size measurement and image-based lasing threshold measurement.

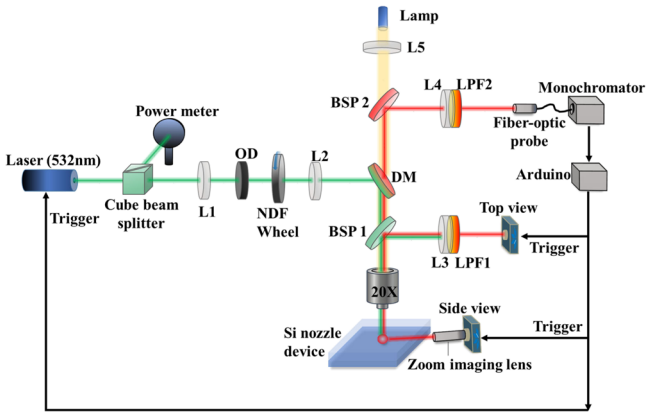

Figure 3. Experimental setup. Laser (532 nm): OPO laser, repetition rate: 2 Hz, pulse width: 5–7 ns, output wavelength: 532 nm. Cube beam splitter: T/R ratio, 50:50. L1–5: lenses with a focal length of 5, 5, 15, 2.5, and 7.5 cm, respectively. BSP1, BSP2: beam splitters with a T/R ratio of 50:50 and 10:90, respectively. OD: neutral density filter with a fixed OD of 1. NDF wheel: neutral density filter wheel with a continuous variable OD from 0 to 2. DM: dichroic mirror with a cutoff wavelength of 550 nm. LPF1, LPF2: long pass filters with a cutoff wavelength of 550 and 600 nm, respectively. Zoom imaging lens: with a variable magnification of 1×–6×. Side-view and top-view cameras are used for monitoring droplets.

Synchronization of Optical Systems. In order to capture the lasing images of the droplet under excitation, a home-built LabView program has been developed to synchronize the monochromator, cameras, and OPO pulsed laser. First, the monochromator is chosen as the master that sends out commands/signals. Second, an Arduino programing board (Arduino Mega 2560) receives the commands from the monochromator and sends out the trigger signals to both top-view and side-view cameras and the OPO pulsed laser, as shown in Figure 3. Through synchronization, each excitation pulse from the OPO laser can be accurately matched to its corresponding lasing emission spectrum and the side-view and top-view images of the droplet.

Formation and Regeneration of Microdroplet Lasers. Nile red (Sigma-Aldrich) is chosen as the organic dye for our laser system. Nile red (500 μM) is dissolved in immersion oil (Sigma-Aldrich, n = 1.515). To generate droplet laser arrays, a positive pressure applied by a high-precision syringe pump (Harvard Apparatus, model 55-1144) pushes the immersion oil from the backside channel to emerge from Si micronozzles to form dye-doped oil droplets in the water environment. The droplet arrays are monitored in real time by the top-view and side-view cameras. The droplet after generation can be studied continuously for a desired period of time, in contrast to the droplet laser on the flow in microfluidic channels. To regenerate droplet laser arrays, a water stream is initiated to wash away the droplets on the micronozzles, and new droplets subsequently form under the positive backside channel pressure. The contact angles (CAs) of droplets of different sizes, 126, 175, 233, and 303 μm in diameter, generated by the micronozzle are characterized in Figure 1d–g. The CA of all the droplets is above 150°, which indicates a good Q factor of microdroplet cavities.

RESULTS AND DISCUSSION

First, the lasing threshold of individual droplets from the droplet laser array is investigated. One of the nozzles is centered under the excitation beam through the top-view camera. For each pump pulse excitation, the top-view image, side-view image, and emission spectrum of the droplet are simultaneously acquired at 2 Hz. The generation and excitation of different sizes of droplets are shown in Figure 4a, in which the sizes of droplets 1–6 are 132, 172, 183, 194, 215, and 284 μm, respectively, as measured by the side-view camera. All

https://dx.doi.org/10.1021/acsami.0c05967
ACS Appl. Mater. Interfaces 2020, 12, 26936–26942

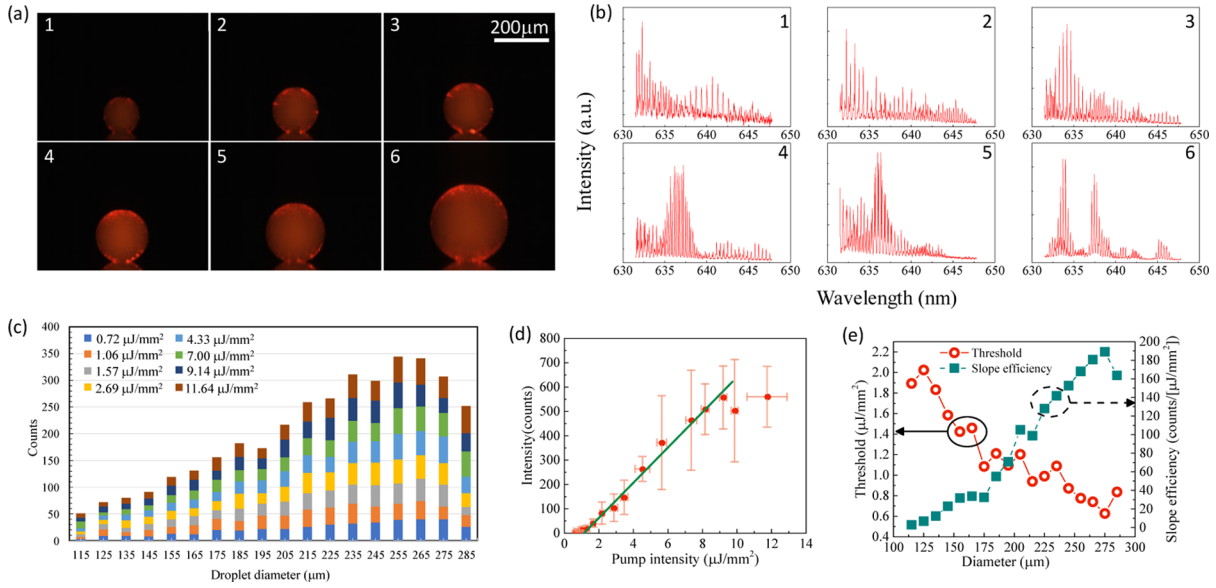

Figure 4. (a) Side-view images of droplets 1−6 under excitation. Droplet diameters are 132, 172, 183, 194, 215, and 284 μm, respectively. For each droplet, excitation energy densities are 7.5, 11.3, 11.1, 8.4, 12.0, and 10.7 μJ/mm^2, respectively. (b) Lasing spectra of droplets 1−6 in (a). (c) Histogram of the droplet size distribution under different excitation energy densities. (d) Lasing threshold of 195 μm diameter droplets, which is 1.09 μJ/mm^2. (e) Lasing threshold and slope efficiency for different sizes of droplets. The overall lasing threshold is in the range of 0.63−2.02 μJ/mm^2.

droplets show a strong lasing emission when they are pumped well beyond their lasing thresholds. The excitation light energy densities for these droplets are 7.5, 11.3, 11.1, 8.4, 12.0, and 10.7 μJ/mm^2, respectively. The corresponding emission spectra from each droplet are measured in Figure 4b. Additionally, the lasing emission can be clearly seen at the droplet circumference in the side-view images in Figure 4a, confirming the surface nature of the WGMs. Based on the free spectral range (FSR) measured from the lasing emission spectrum, the droplet size can be calculated using equation $\Delta\lambda = \lambda_L^2/\pi dm$, in which $\Delta\lambda$ is the FSR, λ_L is the lasing wavelength (λ_L = 640 nm), d is the droplet diameter, and m is the effective refractive index of the WGMs ($m \approx 1.515$). The calculated droplet sizes are 133, 170, 187, 196, 220, and 281 μm, respectively. The difference in sizes measured by the camera and the FSR is less than 2%. Multimodal lasing is observed in individual droplets, as shown in Figure 4b. It is challenging to see well-structured WGMs in the emission spectrum because of the mode competition in these relatively large size droplets. In addition to measuring individual droplets one at a time, synchronization of the experimental setup allows us to characterize a large number of droplets generated by the nozzle continuously. In such continuous mode, the droplet grows to 285 μm in diameter before being released from the nozzle and is regenerated. During the growth period, the lasing emission from the droplet is acquired at 2 Hz. The excitation laser intensity is gradually increased from 0.72 to 11.64 μJ/mm^2 for different rounds of the generation process. The histogram of the droplet size distribution under various excitation power densities is shown in Figure 4c. The lasing emission from a total number of 3650 droplets is characterized in a relatively short period of time. The droplet size is measured using a home-developed MATLAB program, which is shown in Figure S1. Within each size group, the droplet lasing threshold is measured. Because of high-throughput generation, the average and standard deviation of the lasing emission intensity for each droplet size can be easily obtained, which improves the measurement accuracy of the lasing threshold. Figure 4d shows the relationship between the integrated lasing intensity and pump intensity for droplets of 195 μm in diameter (total number of droplets, N = 173). The lasing threshold extrapolated from the linear fitting is 1.09 μJ/mm^2. After applying the same process to other sizes of droplets, the relationship between the lasing threshold and droplet size is presented in Figure 4e. The overall average lasing threshold is in the range of 0.63−2.02 μJ/mm^2. Based on the laser theory, the lasing threshold, $I_{pump(th)}$, is determined by the following equations.[5,39,40]

$$I_{th} = \frac{\gamma}{1-\gamma} \tag{1}$$

where γ is the fraction of gain molecules in the excited state at the threshold and is expressed by

$$\gamma = \frac{\sigma_a(\lambda_L)}{\sigma_e(\lambda_L) + \sigma_a(\lambda_L)}\left[1 + \frac{Q_{abs}}{Q_0}\right] \tag{2}$$

where $\sigma_e(\lambda_L)$ ($\sigma_a(\lambda_L)$) is the dye emission cross section (dye absorption cross section) at the lasing wavelength λ_L, Q_0 is the microdroplet empty-cavity quality factor, and $Q_{abs} = 2\pi m/\lambda_L n_t \sigma_a(\lambda_L)$ is the quality factor related to the dye absorption. n_t is the total concentration of the dye. If the empty-cavity quality factor Q_0 remains the same for all droplets, the lasing threshold should also remain the same for all droplets with different sizes. However, for our laser system, because the droplet is in contact with the Si nozzle surface, the contact area relative to the droplet size can affect the Q factor. For smaller droplets, the contact area between the droplets and Si nozzle surface is relatively large compared to the droplet; thus, the Q factor is lower and the lasing threshold is higher than those of the bigger droplets. Meanwhile, when droplets grow bigger in size, more dye molecules are located near the droplet surface and interact with the WGMs. Therefore, the output lasing intensity increases. As a result, with the increase of the droplet size, the

https://dx.doi.org/10.1021/acsami.0c05967
ACS Appl. Mater. Interfaces 2020, 12, 26936−26942

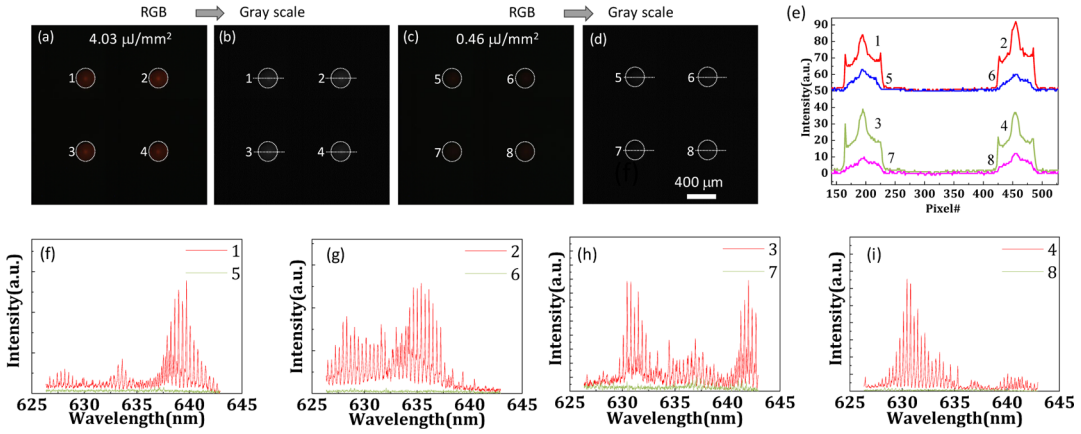

Figure 5. Characterization of the droplet laser array. (a,c) Images of a 275 μm diameter droplet laser array excited with pump power densities of 4.03 and 0.46 μJ/ mm^2, respectively. (b,d) Gray-scale images of (a,c), respectively. (e) Intensity plot of each pixel along the dotted straight line. (f–i) Emission spectra of each droplet under excitation power density above and below the lasing threshold, respectively.

lasing threshold slope efficiency increases linearly and the lasing threshold decreases slightly, as shown in Figure 4e.

We further investigate the lasing emission from the droplet laser array. Because of the 2 × 2 nozzle array design, the OPO laser beam is expanded to excite all four nozzles at the same time. The top-view camera is in use to monitor the droplet size because the side-view camera is not able to keep all four nozzles in focus at the same time. Figure 5a,c shows RGB images of the droplet array under excitation. The pump intensities are 4.03 μJ/mm^2 in Figure 5a and 0.46 μJ/mm^2 in Figure 5c, which are above and below the lasing threshold, respectively. After converting the RGB images of droplets into gray-scale images, as shown in Figure 5b,d, the pixel intensity profiles can be extracted. To examine the light emission from the droplet, the pixel intensity along the straight dashed line which runs through the center of each droplet is plotted in Figure 5e. The center and edge of a droplet are determined using our home-written MATLAB program (see the Supporting Information for details). As shown in the pixel intensity profiles, when the pump intensity is above the lasing threshold of 1.17 μJ/mm^2, high-intensity pixels emerge near the surface on both sides of the droplet (red and light green curves in Figure 5e); when the pump intensity is below the lasing threshold, no high-intensity pixels are observed (blue and magenta curves in Figure 5e). This demonstrates that it is feasible to extract lasing information by utilizing the pixel intensity near the droplet surface. To confirm the results obtained by the camera pixel plot, the light emission from the droplets is concurrently measured by a high-resolution spectrometer. Figure 5f–i shows the emission spectra from these four droplets that are excited above and below the lasing threshold. Furthermore, because the traditional way of measuring the lasing threshold is to obtain multiple emission spectra of the sample under different pump intensities and then linearly fit the relationship between the integrated lasing intensity and pump intensity to estimate the lasing threshold, a spectrometer/monochromator is necessary for the experiment despite their high cost. In order to develop an easy and low-cost method to measure the lasing threshold without involving any spectrometer, we decided to use cameras to achieve this goal, which are generally cheaper than spectrometers. We named this method as the image-based lasing threshold analyzing method. In our work, the images of all excited droplets are processed by our home-built MATLAB program, and then the relationship between the integrated lasing pixel intensity around the edges of droplets and the pump intensity is studied. Because of the resolution of the camera (600 × 800), each pixel is 4 μm in length or width. In order to determine the cutoff value of the pixel intensity between the fluorescence emission and lasing emission, the pixel intensity distribution of the lasing droplet is plotted in Figure 6a,b.

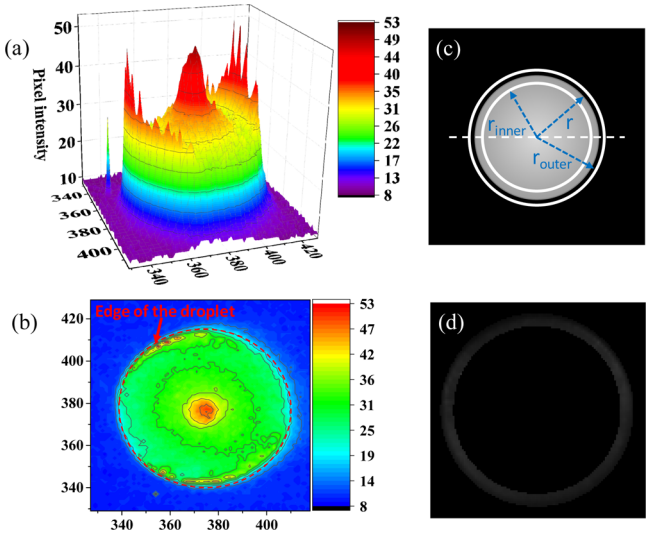

Figure 6. (a) 3D surface and (b) contour plot for droplet pixel intensity distribution. (c) Only pixels within the ring area near the droplet edge are considered for the image-based lasing threshold analyzing method. r is the MATLAB-measured radius, $r_{inner} = r - 4$ (pix), $r_{outer} = r + 3$ (pix). (d) Only pixels that are within the ring area are selected for further analysis.

Along the droplet edge, some pixels present high intensities compared to the remaining pixels, which indicate that those high-intensity pixels contribute to the lasing emission and the remaining pixels present fluorescence emission. The average pixel intensity of fluorescence emission pixels is 21 along the droplet edge, as shown in Figure 6b; thus, this is set as the cutoff value to differentiate pixels for lasing and pixels for fluorescence. Besides, because the lasing emission is coming from WGMs and they only happen near the inner surface of the droplet, only a ring area is chosen for the lasing analysis.

https://dx.doi.org/10.1021/acsami.0c05967
ACS Appl. Mater. Interfaces 2020, 12, 26936–26942

The radius of the outer ring (r_{outer}) is r + 3 pixels (r is the MATLAB-measured droplet radius) and the radius of the inner ring (r_{inner}) is r − 4 pixels, which are enough to include all the possible pixels for the lasing emission. After applying the ring area to the droplet's gray-scale image, the actual area that is considered for lasing analysis is shown in Figure 6d. During the image-based lasing threshold analyzing method, all the pixels within the ring area are subtracted by the cutoff pixel value, and then all the positive values are integrated as pixel lasing intensities. The droplet size distribution is shown in Figure S2 from 245 to 455 μm with a total number range of 40−160. Within each group, droplets are tested under different pump intensities from 0.31 to 5.58 μJ/mm^2. The relationship between the integrated lasing intensity (from the spectrum-based method) and pump intensity is presented in Figure 7a

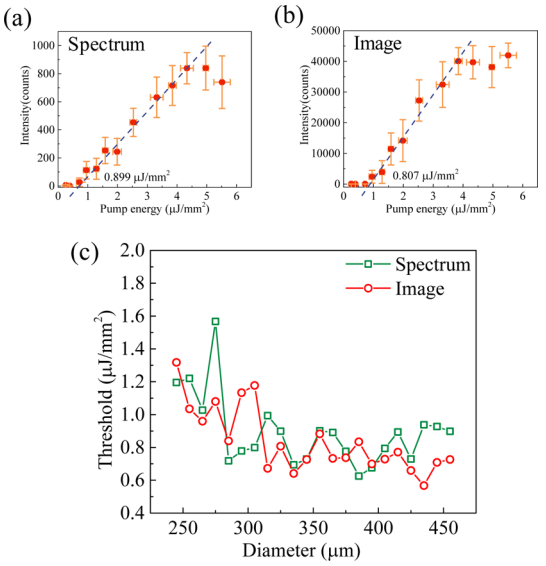

Figure 7. (a) Relationship between the integrated lasing intensity from the emission spectrum and the pump energy for 325 μm droplets. Through linear fitting, the estimated threshold is 0.889 μJ/mm^2. (b) Relationship between the integrated pixel intensity from the equator part of the droplet image and the pump energy for 325 μm droplets. Through linear fitting, the estimated threshold is 0.807 μJ/mm^2. (c) Lasing thresholds for droplets with different sizes. Curve "spectrum" is calculated from the spectrum-based method; curve "image" is calculated from the image-based method.

for 325 μm droplets. The estimated lasing threshold through linear fitting is around 0.899 μJ/mm^2. In comparison, the relationship between the integrated lasing pixel intensity (from the image-based method) and pump intensity is presented in Figure 7b for 325 μm droplets. The estimated lasing threshold through linear fitting is around 0.807 μJ/mm^2. After applying both the spectrum-based method and image-based method to all the droplets, the threshold versus diameter relationship is presented in Figure 7c. The curve "spectrum" shows the lasing thresholds that come from the spectrum-based method with an average threshold of 0.894 ± 0.215 μJ/mm^2, and the curve "image" shows the lasing thresholds that come from the image-based method with an average threshold of 0.838 ± 0.197 μJ/mm^2. The image-based method produces an average lasing threshold that is within 6.68% difference of the average lasing threshold from the spectrum-based method, which shows the good repeatability and reliability of the image-based method for lasing threshold measurements. We admit that the current image-based method is limited by the resolution of the camera. If the resolution is further increased, the analysis for the droplet edges will be more accurate, and even a smaller ring thickness is needed for pixel intensity integration.

CONCLUSIONS

In summary, we have demonstrated a droplet-based laser array and characterized the lasing threshold for droplets with a size of 115−475 μm to be from 0.63 to 2.02 μJ/mm^2. An image-based lasing threshold analyzing method has been developed to characterize the droplet laser array in a fast and cost-effective manner. Our optofluidic droplet laser array can be optically pumped by a compact nanosecond pulsed microchip laser, instead of a bulky and expensive OPO, which makes the laser platform suitable to be used in point-of-care applications. The 2 × 2 droplet laser array can be readily scaled up to a $N \times M$ nozzle array (where N and M are integers), which can be a useful platform for creating an integrated coherent light source on a chip and high-throughput intracavity biosensing using the lasing emission from individual droplets in the array. By changing the backside channel configuration and introducing independent control on the subset of nozzles, different gain media covering different emission spectral regions can be achieved with this laser system, which enables the applications that require multiple operating channels, such as high-speed wavelength switching light sources and on-chip spectroscopic analysis.

ASSOCIATED CONTENT

Supporting Information

The Supporting Information is available free of charge at https://pubs.acs.org/doi/10.1021/acsami.0c05967.

Image processing of droplet size measurement and droplet size distribution in the image-based threshold analysis method (PDF)

AUTHOR INFORMATION

Corresponding Author

Yuze Sun − *Department of Electrical Engineering, University of Texas at Arlington, Arlington, Texas 76019, United States;* orcid.org/0000-0001-5149-2277; Email: sun@uta.edu

Authors

Han Zhang − *Department of Electrical Engineering, University of Texas at Arlington, Arlington, Texas 76019, United States*

Prithviraj Palit − *Department of Electrical Engineering, University of Texas at Arlington, Arlington, Texas 76019, United States*

Yonghao Liu − *Department of Electrical Engineering, University of Texas at Arlington, Arlington, Texas 76019, United States*

Seyedmohsen Vaziri − *Department of Electrical Engineering, University of Texas at Arlington, Arlington, Texas 76019, United States*

Complete contact information is available at: https://pubs.acs.org/10.1021/acsami.0c05967

Notes

The authors declare no competing financial interest.

ACKNOWLEDGMENTS

This research work was supported by the National Science Foundation (1554013).

REFERENCES

(1) Vezenov, D. V.; Mayers, B. T.; Conroy, R. S.; Whitesides, G. M.; Snee, P. T.; Chan, Y.; Nocera, D. G.; Bawendi, M. G. A Low-threshold, High-efficiency Microfluidic Waveguide Laser. *J. Am. Chem. Soc.* **2005**, *127*, 8952−8953.

(2) Tang, S. K. Y.; Li, Z.; Abate, A. R.; Agresti, J. J.; Weitz, D. A.; Psaltis, D.; Whitesides, G. M. A Multi-color Fast-switching Microfluidic Droplet Dye Laser. *Lab Chip* **2009**, *9*, 2767−2771.

(3) Suter, J. D.; Sun, Y.; Howard, D. J.; Viator, J. A.; Fan, X. PDMS Embedded Opto-fluidic Microring Resonator Lasers. *Opt. Express* **2008**, *16*, 10248−10253.

(4) Li, Z.; Zhang, Z.; Emery, T.; Scherer, A.; Psaltis, D. Single Mode Optofluidic Distributed Feedback Dye Laser. *Opt. Express* **2006**, *14*, 696−701.

(5) Sun, Y.; Fan, X. Distinguishing DNA by Analog-to-Digital-like Conversion by Using Optofluidic Lasers. *Angew. Chem.* **2012**, *124*, 1262−1265.

(6) Chen, Q.; Zhang, X.; Sun, Y.; Ritt, M.; Sivaramakrishnan, S.; Fan, X. Highly Sensitive Fluorescent Protein FRET Detection Using Optofluidic Lasers. *Lab Chip* **2013**, *13*, 2679−2681.

(7) Fan, X.; Yun, S.-H. The Potential of Optofluidic Biolasers. *Nat. Methods* **2014**, *11*, 141−147.

(8) Chen, Y.-C.; Tan, X.; Sun, Q.; Chen, Q.; Wang, W.; Fan, X. Laser-emission Imaging of Nuclear Biomarkers for High-contrast Cancer Screening and Immunodiagnosis. *Nat. Biomed. Eng.* **2017**, *1*, 724−735.

(9) Wang, W.; Zhou, C.; Zhang, T.; Chen, J.; Liu, S.; Fan, X. Optofluidic laser array based on stable high-Q Fabry-Pérot microcavities. *Lab Chip* **2015**, *15*, 3862−3869.

(10) Zhen, B.; Chua, S.-L.; Lee, J.; Rodriguez, A. W.; Liang, X.; Johnson, S. G.; Joannopoulos, J. D.; Soljačić, M.; Shapira, O. Enabling Enhanced Emission and Low-threshold Lasing of Organic Molecules Using Special Fano Resonances of Macroscopic Photonic Crystals. *Proc. Natl. Acad. Sci. U.S.A.* **2013**, *110*, 13711−13716.

(11) Shivakiran Bhaktha, B. N.; Bachelard, N.; Noblin, X.; Sebbah, P. Optofluidic Random Laser. *Appl. Phys. Lett.* **2012**, *101*, 151101.

(12) Maeda, M.; Miyawaki, S.; Abe, A.; Oki, Y.; Watanabe, H.; Tanaka, M. *Multi-Channel DFB Dye Laser Covering 560−1100 nm and Rapid Thermal Wavelength Switching*. CLEO 2004; IEEE: Washington DC, 2004, paper CThT64.

(13) Kuehne, A. J. C.; Gather, M. C.; Eydelnant, I. A.; Yun, S.-H.; Weitz, D. A.; Wheeler, A. R. A Switchable Digital Microfluidic Droplet Dye-laser. *Lab Chip* **2011**, *11*, 3716−3719.

(14) Watanabe, T.; Abe, H.; Nishijima, Y.; Baba, T. Array Integration of Thousands of Photonic Crystal Nanolasers. *Appl. Phys. Lett.* **2014**, *104*, 121108.

(15) Oki, Y.; Miyawaki, S.; Maeda, M.; Tanaka, M. Spectroscopic Applications of Integrated Tunable Solid-state Dye Laser. *Opt. Rev.* **2005**, *12*, 301.

(16) Omi, S.; Watanabe, H.; Yang, Y.; Oki, Y. Development of Multicolor DFB Dye Laser by Transversal Quasi-Mode-Coupling Method. *Conference on Lasers and Electro-Optics/Pacific Rim*; Optical Society of America, 2009, paper WD2_2.

(17) Oki, Y.; Kataoka, S.; Kamogawa, N.; Watanabe, H.; Yamashita, K.; Miyazaki, M. Integration of Multiple-DFB Dye Lasers and Microflow-Channel on a Polymeric Chip. *Advanced Solid-State Photonics*; Optical Society of America, 2008, paper MB3.

(18) Lee, S. J.; Lee, S. Y. Micro Total Analysis System (μ-TAS) in Biotechnology. *Appl. Microbiol. Biotechnol.* **2004**, *64*, 289−299.

(19) Iqbal, M.; Gleeson, M. A.; Spaugh, B.; Tybor, F.; Gunn, W. G.; Hochberg, M.; Baehr-Jones, T.; Bailey, R. C.; Gunn, L. C. Label-free Biosensor Arrays Based on Silicon Ring Resonators and High-speed Optical Scanning Instrumentation. *IEEE J. Sel. Top. Quantum Electron.* **2010**, *16*, 654−661.

(20) Wondimu, S. F.; Hippler, M.; Hussal, C.; Hofmann, A.; Krämmer, S.; Lahann, J.; Kalt, H.; Freude, W.; Koos, C. Robust Label-free Biosensing Using Microdisk Laser Arrays with On-chip References. *Opt. Express* **2018**, *26*, 3161−3173.

(21) Oki, Y.; Miyamoto, S.; Maeda, M.; Vasa, N. J. Multiwavelength Distributed-feedback Dye Laser Array and Its Application to Spectroscopy. *Opt. Lett.* **2002**, *27*, 1220−1222.

(22) Tang, S. K. Y.; Derda, R.; Quan, Q.; Lončar, M.; Whitesides, G. M. Continuously Tunable Microdroplet-laser in a Microfluidic Channel. *Opt. Express* **2011**, *19*, 2204−2215.

(23) Zhang, H.; Sun, Y. Optofluidic Droplet Dye Laser Generated by Microfluidic Nozzles. *Opt. Express* **2018**, *26*, 11284−11291.

(24) Kiraz, A.; Kurt, A.; Dündar, M. A.; Demirel, A. L. Simple Largely Tunable Optical Microcavity. *Appl. Phys. Lett.* **2006**, *89*, 081118.

(25) Yang, S.; Wang, Y.; Chen, R.; He, T.; Demir, H. V.; Sun, H. Reconfigurable Liquid Whispering Gallery Mode Microlasers. *Sci. Rep.* **2016**, *6*, 27200.

(26) Li, X.; Qin, Y.; Tan, X.; Chen, Y.-C.; Chen, Q.; Weng, W.-H.; Wang, X.; Fan, X. Ultrasound Modulated Droplet Lasers. *ACS Photonics* **2019**, *6*, 531−537.

(27) Kiraz, A.; Karadag, Y.; Yorulmaz, S. C.; Muradoglu, M. Reversible Photothermal Tuning of a Salty Water Microdroplet. *Phys. Chem. Chem. Phys.* **2009**, *11*, 2597−2600.

(28) Richter, D.; Marinčič, M.; Humar, M. Optical-resonance-assisted Generation of Super Monodisperse Microdroplets and Microbeads with Nanometer Precision. *Lab Chip* **2020**, *20*, 734−740.

(29) Tanyeri, M.; Perron, R.; Kennedy, I. M. Lasing Droplets in a Microfabricated Channel. *Opt. Lett.* **2007**, *32*, 2529−2531.

(30) Zheng, L.; Zhi, M.; Chan, Y.; Khan, S. A. Embedding Liquid Lasers Within or Around Aqueous Microfluidic Droplets. *Lab Chip* **2018**, *18*, 197−205.

(31) Azzouz, H.; Alkhafadiji, L.; Balslev, S.; Johansson, J.; Mortensen, N. A.; Nilsson, S.; Kristensen, A. Levitated Droplet Dye Laser. *Opt. Express* **2006**, *14*, 4374−4379.

(32) Özelci, E.; Aas, M.; Jonáš, A.; Kiraz, A. Optofluidic FRET Microlasers Based on Surface-supported Liquid Microdroplets. *Laser Phys. Lett.* **2014**, *11*, 045802.

(33) Aas, M.; Jonáš, A.; Kiraz, A. Lasing in Optically Manipulated, Dye-doped Emulsion Microdroplets. *Opt. Commun.* **2013**, *290*, 183−187.

(34) Ta, V. D.; Chen, R.; Sun, H. D. Tuning Whispering Gallery Mode Lasing from Self-assembled Polymer Droplets. *Sci. Rep.* **2013**, *3*, 1362.

(35) Humar, M.; Hyun Yun, S. Intracellular Microlasers. *Nat. Photonics* **2015**, *9*, 572−576.

(36) Kiraz, A.; Sennaroglu, A.; Doğanay, S.; Dündar, M. A.; Kurt, A.; Kalaycıoğlu, H.; Demirel, A. L. Lasing from Single, Stationary, Dye-doped Glycerol/water Microdroplets Located on a Superhydrophobic Surface. *Opt. Commun.* **2007**, *276*, 145−148.

(37) Maayani, S.; Martin, L. L.; Carmon, T. Water-walled Microfluidics for High-optical Finesse Cavities. *Nat. Commun.* **2016**, *7*, 10435.

(38) Avino, S.; Krause, A.; Zullo, R.; Giorgini, A.; Malara, P.; De Natale, P.; Loock, H. P.; Gagliardi, G. Direct Sensing in Liquids Using Whispering-gallery-mode Droplet Resonators. *Adv. Opt. Mater.* **2014**, *2*, 1155−1159.

(39) Chen, Q.; Ritt, M.; Sivaramakrishnan, S.; Sun, Y.; Fan, X. Optofluidic Lasers with a Single Molecular Layer of Gain. *Lab Chip* **2014**, *14*, 4590−4595.

(40) Siegman, A. E. *Lasers*; University Science Books: Mill Valley, 1986; p 1283.

https://dx.doi.org/10.1021/acsami.0c05967
ACS Appl. Mater. Interfaces 2020, 12, 26936−26942